Sub-micrometer particle size effects on metastable phases for a photoswitchable Co–Fe Prussian blue analog

Miho Itoi, Isabelle Maurin, Kamel Boukheddaden, Matthew Andrus, Daniel Talham, Erik Elkaim, Yoshiya Uwatoko

Sub-micrometer particle size effects on metastable phases for a photoswitchable Co–Fe Prussian blue analog

Miho Itoi,[1,a)] Isabelle Maurin,[2,3] Kamel Boukheddaden,[4] Matthew J. Andrus,[5] Daniel R. Talham,[5] Erik Elkaim,[6] and Yoshiya Uwatoko[7]

AFFILIATIONS

[1]Division of Physics, Institute of Liberal Education, Nihon University School of Medicine, Itabashi-Ku, Tokyo 173-8610, Japan

[2]Physique de la Matière Condensée, Ecole Polytechnique, CNRS, IP Paris, 91128 Palaiseau, France

[3]Univ. Grenoble Alpes, CNRS, Grenoble INP, Institut NEEL, BP 166, 38042 Grenoble, France

[4]Groupe d'Etudes de la Matière Condensée, UMR 8635, CNRS, Université de Versailles-Saint-Quentin, 45, Avenue des Etats-Unis, 78035 Versailles Cedex, France

[5]Department of Chemistry, University of Florida, P.O. Box 117200, Gainesville, Florida 32611-7200, USA [6]Synchrotron SOLEIL, L'orme des Merisiers, Saint Aubin BP 48, 91192 Gif sur Yvette, France [7]Institute for Solid State Physics, The University of Tokyo, Kashiwanoha 5-1-5, Kaashiwa, Chiba, Japan

a)Author to whom correspondence should be addressed: itoi.miho@nihon-u.ac.jp

ABSTRACT

Metastable phases of the photoswitchable molecular magnet $K_{0.3}Co[Fe(CN)_6]_{0.77} \cdot nH_2O$ in sub-micrometer particles have been structurally investigated by synchrotron powder x-ray diffraction (PXRD) measurements. The $K_{0.3}Co[Fe(CN)_6]_{0.77} \cdot nH_2O$ bulk compound (studied here with a sample having average particle size of 500 nm) undergoes a charge transfer coupled spin transition (CTCST), where spin configurations change between a paramagnetic Co^{II} ($S = 3/2$) $-Fe^{III}$ ($S = 1/2$) high-temperature (HT) state and a diamagnetic Co^{III} ($S = 0$) $-Fe^{II}$ ($S = 0$) low-temperature (LT) state. The bulk compound exhibits a unique intermediate (IM) phase, which corresponds to a mixture of HT and LT spin states that depend on the cooling rate. Several hidden metastable HT states emerge as a function of thermal and photo stimuli, namely: (1) a quench (Q) state generated from the HT state by flash cooling, (2) a LTPX state obtained by photoexcitation from the LT state derived by thermal relaxation from the Q state, and (3) an IMPX state accessed by photo-irradiation from the IM state. A sample with a smaller particle size, 135 nm, is investigated for which the particles are on the scale of the coherent LT domains in the IM phase within the larger 500 nm sample. PXRD studies under con- trolled thermal and/or optical excitations have clarified that the reduction of the particle size profoundly affects the structural changes associated with the CTCST. The unusual IM state is also observed as segregated domains in the 135 nm particle, but the col- lective structural transformations are more hindered in small particles. The volume change decreases to $2\% - 3\%$, almost half the value found for 500 nm particles ($5\% - 8\%$), even though the linear thermal expansion coefficients are larger for the smaller particles. Furthermore, photoexcitation from the IM and LT states does not turn into single phases in the smaller particles, presumably because of the multiple interfaces and/or internal stress generated by the coexistence of small $Co^{II}-Fe^{III}$ and $Co^{III}-Fe^{II}$ domains in the lattice. Since the reduced particle size limits cooperativity and domain growth in the lattice, CTCST in the small particle sample becomes less sensitive to external stimuli.

I. INTRODUCTION

Controlling the size or shape of nano- to mesoscopic-scale particles can lead to the emergence of new material functionalities.[1] Beyond quantum confinement effects, size reduction increases the number of high energy state atoms at the surface and, as a result, properties related to the particle stiffness and electron–phonon interactions in the solid lattice may be altered as the surface-to-volume ratio increases. In the case of coordination polymers, whose flexible framework and porous structures control their functionalities, downsizing to the nanoscale has a strong impact on practical applications,[2] such as catalysis, electrochemistry, or gas storage.

Prussian blue analogs (PBAs) are prototypical porous coordination polymer solids and have attracted considerable attention for their storage[3] and sensor properties,[4] zero/negative thermal expansion,[5] second harmonic generation,[6] and photo-switchable magnetism.[7] Recently, the control over morphology[8] has gained attention as a route to increase the functionalities in PBAs and other network solids, in general. Better physical and structural understandings of how PBAs are altered at the nano- and mesoscopic scale are needed to under- stand the consequences of complex architectures, such as epitaxially grown core–shell nanoparticles, meso-structural PBA particles,[9] and artificial processing on PBA particles,[10] on physical phenomena.

Cobalt hexacyanoferrates,[7(a)–7(e),11] CoFe-PBAs, are well-studied light-switchable molecular magnets, whereby magnetization is altered by thermal or optical excitation between a Fe^{III} ($S = 1/2$)–Co^{II} ($S = 3/2$) high–temperature (HT) spin configuration and a diamagnetic Fe^{II} ($S = 0$)–Co^{III} ($S = 0$) low-temperature (LT) spin configuration. Traditionally referred to as a charge-transfer induced spin transition (CTIST), a recent study showed the spin-state change precedes the charge transfer in at least one example.[12] Therefore, we will refer to this process as a charge transfer coupled spin transition (CTCST), understanding it is the same process referred to the earlier literature as CTIST. The CTCST is accompa- nied by a large lattice volume change, due to a modification of the Co–N bond distance.

Previous studies[13] showed that a specific composition, $K_{0.3}Co[Fe(CN)_6]_{0.77} \cdot nH_2O$, presents several metastable states as a function of photo-thermal history. Investigations using 500 nm particles showed the formation of an unusual intermediate (IM) state on cooling [$T_{CT1/2\downarrow} \sim 210$ K, see Fig. 1(a)], which corresponds to a mixture of LT-like and residual HT species. At low temperatures, the population ratio derived from PXRD is 30%–40% for the LT-like component, and the residual 60%–70% is a mixed state formed by both LT and HT spin configurations (the former is denoted as IM-B and the latter is called as IM-A in Ref. 13). The estimated domain size of the LT-like (IM-B) is 100–200 nm, while that of the HT-LT mixed species (IM-A) is significantly smaller, ~50 nm, in the IM phase. The thermal CTCST on cooling is quite broad as it spreads over 70–80 K. On the other hand, the CTCST on heating is more abrupt, at $T_{CT1/2\uparrow} \sim 220$ K, irrespective of the nature of the low-temperature phase or of the heating rate. Furthermore, additional phases can be formed at low temperatures depending on sample history, Fig. 1(a). Rapid cooling from ambient temperature produces a quenched phase (Q phase), which is also HT-like. Thermal decay of the Q phase results in an other- wise inaccessible LT phase. Finally, light irradiation of the IM
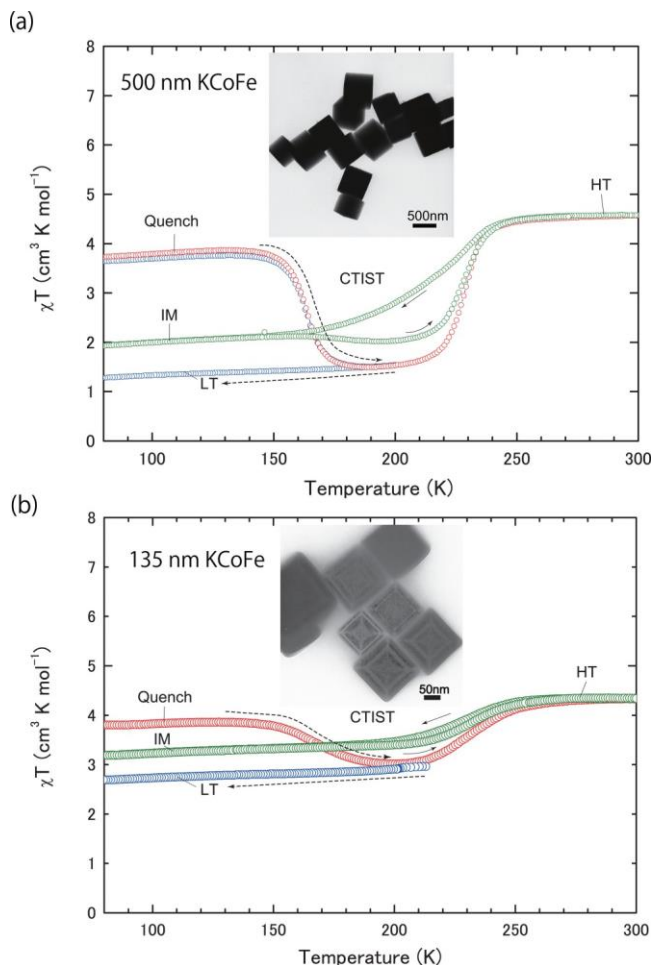

FIG. 1. Magnetic susceptibility curves of $K_{0.3}Co[Fe(CN)_6]_{0.77} \cdot nH_2O$ for (a) 500 nm and (b) 135 nm particles. The thermally accessed Quench (Q) phase and low-temperature (LT) phase are depicted as red and blue curves, respectively. The thermal procedure to reach the LT phase is indicated by dotted arrows. The IM phase is obtained by slow cooling (at 1 K/min). Differences in the thermal response as a function of particle size are observed in the hysteresis, becoming narrower with decreasing particle size. In (a) and (b), $\chi \cdot T$ values were calculated from the same raw magnetic data as those described in Refs. 13 and 15. It should be noted that molar magnetic susceptibilities for the 500 nm and the 135 nm samples were calculated as the molecular weight of $K_{0.4}Co_{1.3}[Fe(CN)_6] \cdot nH_2O$ to compare to the result of Ref. 14. Insets: TEM images of the particles showing their clear cubic shapes.

phase or the LT phase produces other HT-like phases, termed IMPX and LTPX.

To better understand this unusual phase behavior, 135 nm KCoFe-PBA particles were specifically designed to be in a size regime comparable to the sub-structures determined by PXRD in the IM state of the larger particles studied previously. As for the 500 nm particles, multiple phases are once again observed, although with notable differences. Reducing the particle size leads to significant shifts and broadening of most transformation

processes,[14] including the heating branch of the CTCST hysteresis loop and the thermal decay of the HT trapped phase [Fig. 1(b)]. The residual HT fraction is significantly enhanced relative to the larger 500 nm particles, and the CTCST shows a quasi-reversible behavior.

In the present study, we have identified the main structural features of the different metastable phases in 135 nm KCoFe-PBA particles from synchrotron powder x-ray diffraction measurements. We carried out photoexcitation of the 135 nm sample and com- pared the structural transformations of the three metastable HT phases, accessed via thermal or photoexcitation, with those of a 500 nm reference sample. We found that the changes in CTCST behavior with size reduction are correlated to the lattice stretchabil- ity, the decrease in interaction range caused by the weak coopera- tivity of electron−phonon coupling and intrinsic strain produced by small domain segregations, which stabilize the HT spin configuration.

This manuscript is organized as follows: Sec. II presents the experimental techniques and Sec. III gathers the experimental results of thermally- and photo-induced studies using powder x-ray diffraction for the 135 and the 500 nm samples. In Sec. IV, we discuss the unusual IM phases reached by the CTCST from the viewpoints of the intrinsic lattice elasticity and lattice compressions under external pressure using complementary magnetic susceptibil- ity measurements. In Sec. V, we conclude and outline some possi- ble extensions of this work.

II. EXPERIMENTAL SECTION

The synthesis and characterization of the two $K_{0.3}Co[Fe(CN)_6]_{0.77}$ · nH_2O samples are described in Refs. 13 and 14. Their average particle sizes were estimated to be 135 and 472 nm, respectively, from transmission electron microscope (TEM) and scanning electron microscope (SEM) images. The particle size distributions for two samples are shown in Fig. S1 (see in the supplementary material).

A. Photoexcitation and temperature-dependent powder x-ray diffraction

Structural changes in the $K_{0.3}Co[Fe(CN)_6]_{0.77}$ · nH_2O sample under thermal cycling and photoexcitation were investigated by powder x-ray diffraction (PXRD) at the CRISTAL beamline of the SOLEIL synchrotron radiation facility (135 nm sample) and at the Swiss-Norwegian beamlines (station BM1A) at ESRF (500 nm sample). Selected PXRD measurements of the 500 nm sample were already detailed in Refs. 13 and 16. The powders were packed in 0.1 mm diameter glass capillaries. Temperature-regulated N_2 gas was blown directly onto the capillaries using commercially available cryostreams (Oxford cryosystem, 700+ or Cryo Industries of America, Inc). The temperature sweep rate was fixed at 1 K/min. Powder LaB_6 (NIST standard) was used to calibrate the wavelength, sample-to-detector distance, beam center, and tilt angle of the MAR345 image plate detectors. The x-ray wavelength was 0.6687 Å for measurements related to the 135 nm sample and three sets of wavelengths, 0.726 89, 0.711 40, and 0.718 30 Å were used for the 500 nm sample. A same laser diode system ($\lambda = 690$ nm, 35 mW maximum output power) was used at both beamlines, for

irradiations carried out at 100 K for the 135 nm sample and at 80 K for the 500 nm sample. Illumination times needed to complete the transitions ranged from 30 min to 3.75 h: 0.5 h (LTPX), 3.75 h (IMPX) for 135 nm sample, and 1.5 h (LTPX and IMPX) for 500 nm sample.

B. Magnetic susceptibility measurement under pressure

Magnetic susceptibility measurements for the 135 nm KCoFe-PBA sample were carried out with a piston cylinder CuBe pressure cell designed for SQUID magnetometry at ISSP (Institute for Solid State Physics). Fluorinert 70:Fluorinert 77 mixture (1:1) was used as pressure transmitting liquid. About 2 mg of powder sample, which was wrapped in a plastic thin film, was placed between quartz rods (1.5–2 cm), and a Sn shot as a pressure manometer placed at the end of one quartz rod in the CuBe cell. The magnetic moments in CuBe cell were measured by a 4 cm scan with 40-points measured. Pressure was calibrated from the super- conducting temperature of the Sn shot. External pressure was applied up to 0.5 GPa. The magnetic susceptibility was measured from 4 to 300 K at 1 K/min sweep rate. We subtracted the back- ground of the CuBe cell and all parasitic contributions as offset linear values, which were estimated by linear fitting of the $\chi.T$ vs T
plot in the paramagnetic region from ∼50 to ∼180 K (Fig. S2 in the supplementary material).

III. RESULTS

A. Temperature-dependent lattice parameter change for 135 nm KCoFe-PBA

As a complement to magnetization measurements, *in situ* PXRD studies were used as a multiscale technique to probe and quantify segregation processes during phase changes. Although incomplete CTCST has been reported for various CoFe-PBAs,[17] their characterization by PXRD remains limited. Figure 2(a) shows selected PXRD patterns representative of the HT state at 298 K, and the metastable Q, LT and IM states for the 135 nm sample at 100 K. One should refer to Ref. 13 for similar studies conducted for the 500 nm particles. HT- and Q-PXRD profiles are representative of single phases and are compatible with the *fcc* structure character- istic of the three-dimensional Co−NC−Fe network. The lattice parameters, *a*, obtained by the Le Bail method are 10.291 05(7) Å (HT) and 10.239 11(11) Å (Q), while PXRD profiles related to the IM and LT states at 100 K exhibit broad peaks with a poorly resolved line splitting [see Figs. 2(a) and 2(c)], reminiscent of what was observed for the bigger 500 nm particles. [Fig. S3(a) in the supplementary material]

Figure 2(b) shows the temperature dependence of the lattice parameter, *a*, for the different metastable states, which were deter- mined from (400) Bragg reflections. Following the previous PXRD study on 500 nm particles, all states were treated as biphasic, except for when in the high-temperature region and of cubic symmetry (the possibility of symmetry lowering will be discussed in Sec. IV). The lattice constant values at 100 K are listed in Table I, where data related to the 500 nm sample are recalled for a direct comparison.
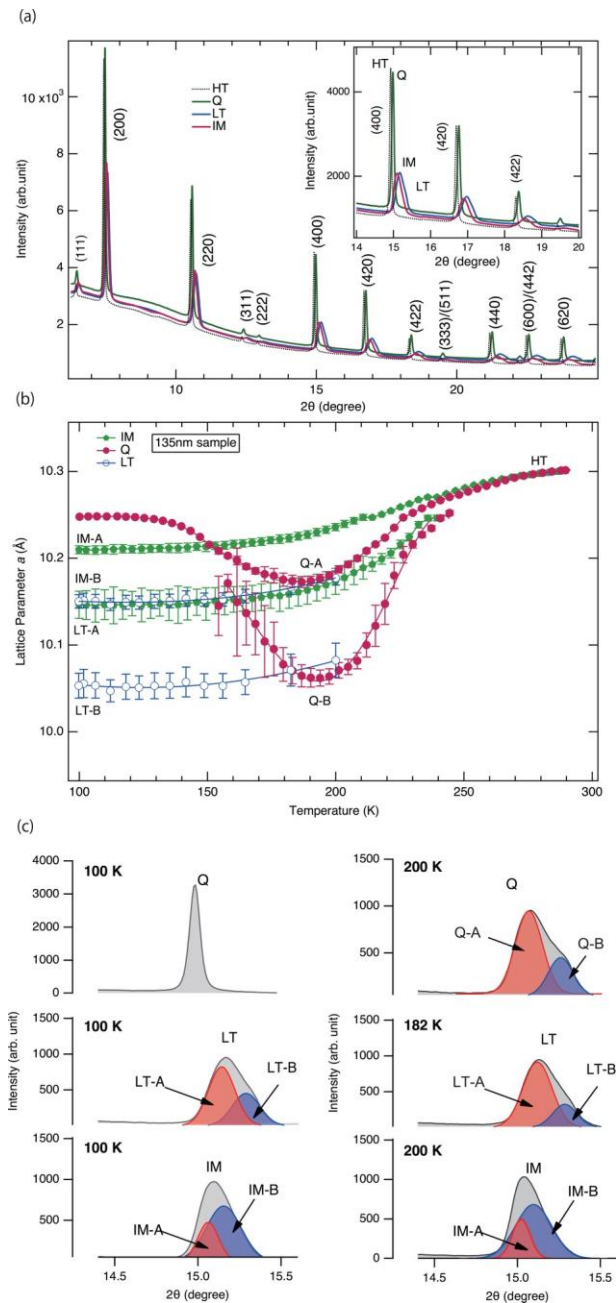
FIG. 2. (a) Synchrotron powder x-ray diffraction (PXRD) profiles of the high-temperature (HT) phase at 298 K and Quench (Q) phase, Intermediate (IM) phase and low-temperature (LT) phase at 100 K for the 135 nm $K_{0.3}Co$ $[Fe(CN)_6]_{0.77} \cdot$ nH_2O particles. (b) Temperature dependences of the cubic lattice parameter, a, estimated from the (400) Bragg peaks. The IM state was measured only during a cooling run. Q phase was obtained by rapid cooling from ambient temperature to 100 K. All PXRD profiles were analyzed as biphasic except for the HT phase. (c) (400) peaks at 100 K (left) and ~ 200 K (right) for the Q, LT and IM states. The (400) reflection in each LT and IM phase, or Q phase at 182 K is broad, and representative of the lattice A (filled red) and lattice B (filled blue).

From the report of the 500 nm particles,[13] the PXRD profile corresponding to the IM state obtained upon cooling was fitted as a two-phase mixture made of 60% IM-A (broad peak at lower 2θ angles) and 40% IM-B (sharp peak at higher 2θ angles). The lattice parameters, a, of these two phases are ~ 10.09 Å (IM-A, unit cell volume $V \sim 1027$ Å^3) and ~ 9.98 Å (IM-B, $V \sim 994$ Å^3), respectively, and the metastable HT lattice corresponds to ~ 10.26 Å (Q state, $V \sim 1080$ Å^3) (see Table I). The IM-B value is larger than the one representative of the single-phase LT state (~ 9.93 Å, $V \sim 979$ Å^3) formed by the decay of the Q phase, which could be due to internal stresses associated with the intergrowth of small and large volume domains. The coherence length obtained using the Stokes–Wilson approach is 50–100 nm for the IM-A domains, and 100–200 nm for IM-B.[13]

Decreasing the size of the KCoFe-PBA particles to 135 nm, i.e., in between the two domain sizes observed for the 500 nm par- ticles, leads to a different approximate-biphasic configuration after cooling to 100 K below the thermal CTCST [Fig. S3(b) in the supplementary material]. For the 135 nm particles, peak profile fits of the IM state (hereafter denoted "@particle size" for state identifi- cation), Fig. 2(c), yields a majority (69%) IM-B@135 nm phase, with a lattice parameter of 10.15 Å, and a minority (31%) IM-A@135 nm with a 10.21 Å lattice constant at 100 K, where A and B again refer to the low-angle and high-angle contributions, respectively. The lattice parameters of the two components were determined from deconvolution of the (400) Bragg peaks by using two pseudo-Voigt functions [Fig. 2(b)]. Gaussian functions were used to determine areas and to compare with the data of the 500 nm sample. (see Table I). Other reflections, (111) and (222) are indicated in Fig. S4 in the supplementary material. The (111) peak position and the FWHM (full width at half maximum) obtained by Gaussian fitting are listed in Table S1 in the supplementary material. Using the Scherrer formula, $D = \frac{K\lambda}{\beta \cos\theta}$ (K: Scherrer cons- tant, β: FWHM, λ: wavelength), the estimated coherence lengths are 30–50 nm for IM-A@135 nm and 15–20 nm for IM-B@135 nm. Decreasing the particle size from 500 to 135 nm not only changes the structure of the domains, but also their size.[18] Note that these characteristic sizes should be considered with caution as part of the diffraction line broadening could result from internal stresses and the fact that CTCST produces a gradient of a-parameters. This latter picture is in better agreement with direct observations made at low temperature by TEM for the 135 nm sample.[15]

These findings suggest that decreasing the particle size has a dramatic influence on phase segregation and implies that the nucle- ation and growth of LT-like domains is severely suppressed in the 135 nm particles. Experimental and theoretical studies on nanome- ter scale PBAs and other spin-crossover particles, with sizes on the order of several tens of nanometers, have indicated surface instabil- ity increases at small sizes favoring trapping high-spin (HS) species at low temperatures.[19] For example, as particle sizes are reduced, the magnitude of the photoinduced magnetization was shown to decrease for photo-switchable RbCoFe-PBA nanoparticles,[20] and the long-range ferrimagnetic order often observed for RbCoFe-PBAs is suppressed below ~ 10 nm particle size.[21] In a study on another PBA, the ferromagnetic CsNiCr-PBA, the small- est single domain particles size is reported as around 14–16 nm.[22] However, the 135 and 500 nm particles in the present study are

TABLE I. Magnetic transition temperature (T_C), relaxation temperature (T_{relax}) of metastable phases, transition temperature of CTCST ($T_{CT1/2}$) obtained by magnetic susceptibility measurement and lattice parameter a for the 500 and the 135 nm samples.[a]

State	500 nm particle					135 nm particle			
	T_C (magnetic susceptibility)[13] (K)	T_{relax} and $T_{CT1/2}$ (magnetic susceptibility)[13] (K)	T_{relax} (PXRD) (K)	Lattice parameter a (100 K) (Å)	Area (%)	T_{relax} and $T_{CT1/2}$ (magnetic susceptibility) (K)	T_{relax} (PXRD) (K)	Lattice parameter a (100 K) (Å)	Area (%)
Q	11–14	160	170[13]	10.2634(63)	100	168	157	10.24	100
LT	…	…	…	9.9345(3)	100	…	…	10.18/10.08	63/37
IM	11	$T_{CT1/2\downarrow}$ 203	…	10.092 49(17)	60	$T_{CT1/2\downarrow}$ 221	…	10.21	31
		$T_{CT1/2\uparrow}$ 229 (CTCST)		9.976 84(112)	40	$T_{CT1/2\uparrow}$ 232 (CTCST)		10.15	69
LTPX	18	130–140	160[13]	10.282 72(18)	100	…	129	10.25/10.17	46/54
IMPX	17	130, 150–170	160/170	10.278 148 (407)	100	…	122/60	10.25/10.19	47/53

[a]T_{relax} values were arbitrarily defined from the inflection points of the $\chi \cdot T$–T curves and a–T curves. Area ratios were estimated by Gaussian fitting of the (400) peak at 100 K for the 500 nm and the 135 nm samples. The lattice parameter at room temperature is 10.306 26(10) Å (500 nm, obtained by Rietveld analysis)[16] and 10.291 05(7) Å (135 nm, obtained by the Le Bail analysis). The lattice parameter for the Q state in the 135 nm sample obtained by the Le Bail method is 10.239 11 (11) Å.
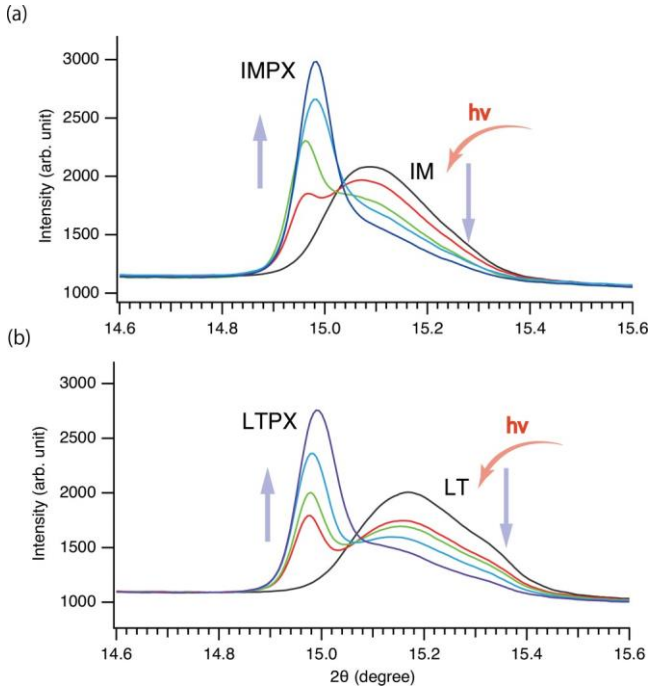

FIG. 3. Photoexcited states in the 135 nm particles produced from IM and LT states by 690 nm light irradiation at 100 K. Complete photoexcitation is not achieved using illumination times common for related analogs.[13,16,23] (a) (400) peak change by photo irradiation from IM to IMPX, following exposure times up to 3.75 h. (b) (400) peak change from LT to LTPX over exposure times of 0.5 h.

well outside of this range. In the case of the title compound with 23% cyanometallate site vacancies, the number of Co and Fe atoms is roughly estimated as $\sim$2:2$\times 10^8$ for the 500 nm sample and $\sim$4:4$\times 10^6$ for the 135 nm sample, if the Co–Fe bond length is considered as $\sim$5 Å. Then the fraction of surface atoms to bulk atoms is 1.2% for the 500 nm particles and 4.4% for the 135 nm samples. The contribution of surface atoms in this size regime is small; therefore, surface instability is not the key factor governing the unusual IM state.

The LT state, derived from relaxing the Q state upon warming, is also observed for the 135 nm particles. However, unlike for the 500 nm particle sample, peak splitting is seen in the 135 nm LT state, that would be representative of phase segregation. Assuming again two phases [Q-A and Q-B, or alternatively LT-A and LT-B, see Figs. 2(b) and 2(c)], the larger lattice constant, 10.18 Å, is assigned as LT-A@135 nm and closely resembles the IM-B@135 nm phase (10.15 Å). The other component, LT-B@135 nm, has a lattice constant of 10.08 Å, closer to, but still somewhat larger than typical low-spin values. Peak deconvolution for the LT state yields 63% LT-A@135 nm and 37% LT-B@135 nm at 100K.

B. Photoexcitation from IM and LT for KCoFe-PBA: Particle size effect

Photoswitching of the 135 nm sample from either the LT or IM states is much less efficient than for the larger particles. Even after 0.5 h (from LT) or 3.75 h (from IM) of light irradiation at 100 K, we could not achieve complete transformation to a single HT metastable phase and the photoexcited states, LTPX and IMPX, both contain segregated domains (Fig. 3). The volume changes associated with the photoinduced CTCST are also small, 1.2% for

the IM-A@135 nm → IMPX-A@135 nm and 2.1% for the LT-A@135 nm → LTPX-A@135 nm transition. The efficiency of photoexcitation and the degree of lattice parameter change could be monitored by Δa = (original state a)–(photo-excited state a), which is plotted vs temperature in Fig. S5 in the supplementary material. For the 135 nm particles, the LT state gets more effectively photo-excited than the IM state (Fig. S5(b) in the supplementary material). The second component in each case, IMPX-B@135 nm and LTPX-B@135 nm gives broad PXRD peaks, which is likely related to the observation that the decay temperatures of the meta- stable IMPX and LTPX states are significantly lower than those of the 500 nm sample, as shown in Fig. 4 and Table I.
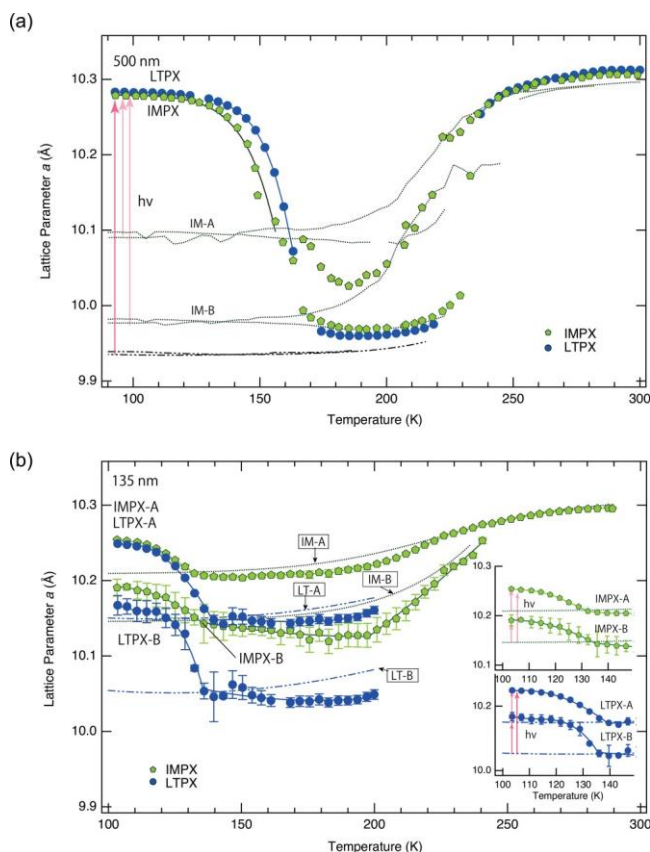

FIG. 4. Thermal decay of the lattice parameter a for photo-excited states IMPX (filled pentagons) and LTPX (filled circles) produced from IM and LT states, at 90 K for the 500 nm sample and at 100 K for the 135 nm sample. (a) Data related to the 500 nm sample extracted by the Le Bail method. The original IM state and LT state, which are the starting phases before 690 nm light irradiations, are indicated by the dotted and dotted-dashed lines, respectively. Data related to LT, LTPX and IM are adapted from Refs. 13 and 16. (b) Similar plots for the 135 nm sample extracted from (400) PXRD peaks. Inset: Expanded figures between 100 and 150 K for temperature-dependent photo-excited lattice parameters, IMPX-A and B (filled pentagons) and LTPX-A and B (filled circles) from the respective original states, IM-A and B (dotted lines) and LT-A and B (dotted-dashed lines).

Structural changes within the IMPX and LTPX phases are summarized in Fig. 4. In the case of the 500 nm sample [Fig. 4(a)], the single IMPX@500 nm photo-excited phase relaxes back to two phases denoted by IM-A and IM-B. Notably, the IM-A phase reached by thermal relaxation of the IMPX state falls to a lower lattice constant than the IM-A in the original IM state (10.09 Å at 167.1 K). On the other hand, the IM-B phase relaxes to almost the same lattice value as the original IM-B@500 nm (9.99 Å at 167.1 K). For the LTPX@500 nm, thermal relaxation returns to near the starting LT@500 nm state.

Clearly, the case of the 135 nm sample is more complex. Upon warming, the lattice parameters a of the biphasic LTPX state return near 140 K to the respective LT-A@135 nm and LT-B@135 nm lattice values of the LT phases before photoexcitation, and then remain nearly constant at ∼10.15 Å for LT-A and ∼10.05 Å for LT-B. For IMPX, lattice relaxation occurs at ∼122 K, below the relaxation temperature of the LTPX state, and values of the two components formed after decay, IMPX-A@135 nm and IMPX-B@135 nm, fall below the values found in the original IM state with continued warming. The a-parameter of IMPX-A@135 nm stabilizes about 150 K, but the one of IMPX-B@135 nm continues to decrease up to 200 K before expanding again and joining the IMPX-A@135 nm curve at around 240 K.

In the 135 nm sample, the onset of the decay of the Q state is at lower temperatures, and the temperature range over which relaxation occurs is wider than in the 500 nm particles. This can be seen both from the magnetic susceptibility curves and from the change of a-parameter on warming. A likely reason for the lower temperature onset for relaxation starting temperature is that the cooperativity of the electron–phonon coupling is reduced in the small particles.

IV. DISCUSSION

CTCSTs were found to be incomplete upon thermal cycling for both 500 and 135 nm samples and also after light irradiation for the 135 nm particles. For the IM phase formed after cooling at low-temperature, PXRD studies reveal the presence of split and poorly resolved peaks for each lattice planes. Two possible reasons of these unusual peak splittings and broadenings after CTCST are considered: (1) it could be due to local symmetry lowering, with structural change restricted to short distances. Reduction from cubic symmetry has been reported for various Prussian blue analogs depending on the nature of the alkali metal ion or in the course of pressure studies, to either monoclinic[24] or rhombohe- dral[25] space groups due to a cooperative tilting of the octahedral units. Symmetry changes can also result from Jahn–Teller effects in the Mn and Cu derivatives.[26,27] From the theoretical point of view, investigations on ferroelastic transitions coupled with symmetry- breaking and volume strain which usually lead to unsymmetrical thermal hysteresis loop in spin-transition materials, have been reported by several authors.[28] Alternatively, (2) these multiple reflections could account for the formation of isolated Co^{II}–Fe^{III} pairs or clusters of pairs within a coherent lattice. This latter picture would be in better agreement with statistical analyses made on low-temperature HR-TEM images at least for the 135 nm sample.[15] Note that a large peak broadening was also emphasized

by Bleuzen and co-workers as a function of alkali metal insertion in Co−Fe PBAs with a maximum FWHM of the (220) lines observed for a Co^{III} fraction of ca. 50%.[29]

Although the possibility of symmetry lowering cannot be ruled out in these KCoFe-PBA samples, we chose to model the PXRD patterns as multiple phases, keeping in mind that the two- phase picture is an approximation for the 135 nm sample (see Fig. 2) intended to facilitate comparison with the data related to the 500 nm particles.

A. Constrained Co^{II}−Fe^{III} spin configurations in the IM phase estimated by magnetic susceptibility measurements

Since the characteristic metastable states of $K_{0.3}Co[Fe(CN)_6]_{0.77}$ · nH_2O are related to the electron−phonon coupling in the elastic Co−Fe framework lattice, size reduction at sub-micrometer scale is
considered to directly relate to the degree of cooperativity. In addition to the differences observed for the temperature sweeps of magnetization (Fig. 1) and PXRD [Fig. 2(b)], size reduction also influences the isothermal relaxation of the metastable HT spin state population vs time, as measured by magnetic susceptibility for the Q phases (Fig. S6 in the supplementary material). The relaxation curves of the 500 nm particles show a clear sigmoidal shape [Fig. S6 (a) in the supplementary material] which is the signature of the presence of long-range elastic interactions dictating the cooperative character of the electronic and structural relaxation of the quenched state. In contrast, for the 135 nm sample, the Co^{II}−Fe^{III} → Co^{III}−Fe^{II} transition occurs gradually compared to the 500 nm sample, and the relaxation curves of the 135 nm samples exhibit a stretched exponential decay [Fig. S6(b) in the supplementary material], which is characteristic of disordered systems with a distribution of energy barriers.

The elastic properties depend on the nature and partitioning of lattice domains having HT and LT spin configurations, leading to different states, depending on history. This point is seen most clearly for the thermal relaxation from photo-excited phases in Fig. 4. After thermal relaxation of the IMPX and LTPX states, the lattice values always shrink below those of the original IM and LT states [Fig. S5(b) in the supplementary material].

It is likely that the segregation of clusters or nano-domains with different local volumes in the 135 nm cubic particle leads to strain, that contributes to part of the peak broadening, leading to Co−Fe bond-lengths in these domains which change continuously in response to the internal stress. Therefore, the IM-B phase is a representative of many Co^{II}−Fe^{III} sites or clusters of sites within a surrounding Co^{III}−Fe^{II} environment that constrains them from fully expanding to equilibrium HT bond lengths. These "con- strained Co^{II}−Fe^{III} clusters" will experience a lower barrier to switching from Co^{II}−Fe^{III} to Co^{III}−Fe^{II}. The situation is reminiscent of core−shell particles where CoFe-PBA core particles are sur- rounded by an isostructural but non-transitioning shell, such as RbCoFe-PBA@KNiCr-PBA nanoparticles, for which it was shown the presence of the shell limits the ability of the CoFe-PBA core to expand and contract during the CTCST.[30,31] A consequence of the constraints induced by the shell in the core−shell particles is a lower barrier to switching between the strained HT and LT

states,[32,33] similar to what is observed in the heterogeneous IM phases of the $K_{0.3}Co[Fe(CN)_6]_{0.77}$ · nH_2O particles studied here.

The percentage of the sample made up of these constrained Co^{II}−Fe^{III} clusters in the 135 nm sample could be estimated based on the magnetic susceptibility and the PXRD data of the 500 and 135 nm samples. The magnetic susceptibility values of the Q (HT spin) state and the LT (LT spin) states at 100 K in the 500 nm sample are 3.8 cm^3 K mol^{-1} and 1.3 cm^3 K mol^{-1}, respectively [Fig. 1(a)], while the corresponding value of the IM phase at 100 K in the 135 nm sample is 3.05 cm^3 K mol^{-1} [Fig. 1(b)]. We assume the IM-A@135 nm phase, which is 31% of the PXRD peak area at 100 K, contains Co^{II}−Fe^{III} clusters and the IM-B@135 nm phase, which is 69% of the PXRD peak area at 100 K, has both of Co^{II}−Fe^{III} and Co^{III}−Fe^{II} clusters. Using the above values and setting the Co^{II}−Fe^{III} : Co^{III}−Fe^{II} ratio as x : $(1-x)$, the "constrained Co^{II}−Fe^{III} clusters" are estimated to makeup ∼57% of the IM-B@135 nm phase. The total Co^{II}−Fe^{III} population in the IM state is estimated as ∼70%, in line with M-H measurements for the Q and IM states, which show the magnetization value at 4500 G of the IM state is about 80% of that of the Q state (see Fig. S7 in the supplementary material).

Although the differences of switching properties as a function of particle size can be rationalized by a change in cooperativity, open questions remain, such as the origin of this inhomogeneous IM phase, which is nearly absent from the related $Na_{0.32}Co[Fe(CN)_6]_{0.74}$ · 3.4H_2O sample with comparable particle sizes, where K is substituted by Na. Nonetheless, observations of anomalies with potentially similar origins should be recalled, such as broadening of the diffraction peaks after cooling below the thermal CTCST, or the fact that the magnetic susceptibility, $\chi.T$, was smaller after the decay of the HT quenched state with respect to the $\chi.T$ value measured for the LT state obtained under slow cooling.[23]

B. Thermal expansion coefficients of the IM phases obtained from x-ray diffraction analyses

Interfaces between Co^{II}−Fe^{III} and Co^{III}−Fe^{II} clusters contribute to internal stress, and as their size, distribution and number are different in the small and larger particles, they will contribute to elasticity differences with size reduction in IM phases. Figures 2(b) and 5(a) show that upon cooling both A and B-components of the 135 nm particle contract, by ∼2% for IM-A@135 nm (between 250 K → 185 K) and ∼3% for IM-B@135 nm, (250 K → 195 K). For comparison, the 500 nm sample exhibits volume changes of ∼5% for IM-A@500 nm (240 K → 171 K) and ∼ 8% for IM-B@500 nm (240 K → 160 K) in the cooling branch of the thermal CTCST, indicating differences in the thermal expansion coefficients for the two particle sizes.

Since the crystal structure of $K_{0.3}Co[Fe(CN)_6]_{0.77}$ · nH_2O remains cubic in the vicinity of the CTCST, the linear thermal expansion coefficient (LTEC) is isotropic, so the temperature-dependent lattice change can be expressed by using a polynomial−sigmoidal function for the spin-crossover transition,[34] which is given as

$$a(T) = a_0 + a_1 T + a_2 T^2 + a_3 T^3 + \frac{a_4}{\left(1 + \exp\left(\frac{(a_5 - T)}{a_6}\right)\right)}. \quad (1)$$
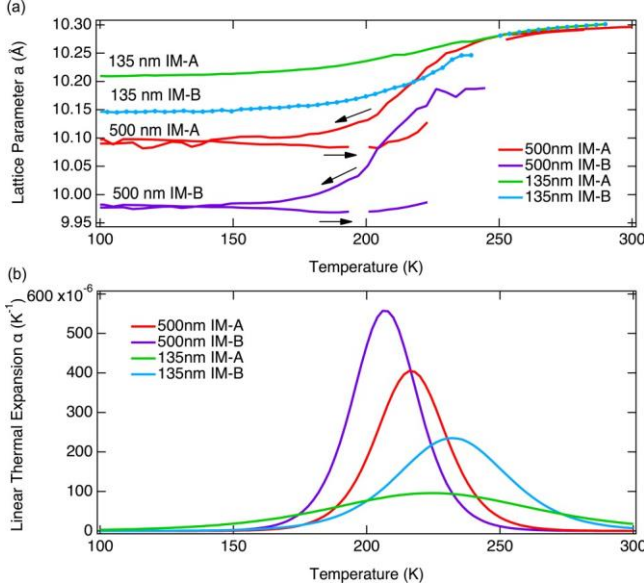
FIG. 5. (a) Temperature-dependent lattice parameter, *a* in the IM phases for 500 and 135 nm samples, derived from a two-phase modeling. The data for the 135 nm sample were obtained from pseudo-Voigt function fitting of the (400) diffraction peak, while the 500 nm particle data were obtained through Le Bail profile fitting. (b) Linear thermal expansion obtained from the cooling cycle by fitting the polynomial plus sigmoidal function for the temperature-dependent lattice parameter change.

The LTEC for KCoFe-PBA is then obtained by

$$\alpha_L = \frac{d}{dT}[\ln(a(T))]: \tag{2}$$

The value of LTEC (α_L) in the IM state vs temperature is plotted in Fig. 5(b) for the cooling branch. First, the plot identifies the inflection points of the temperature-dependent lattice parame- ter change caused by CTCST, estimated as 224.6 K for the IM-A@135 nm phase and 216.7 K for the IM-A@500 nm phase. On the other hand, for IM-B@135 nm and IM-B@500 nm the

inflection points are 232.22 and 207.04 K, respectively. The sharper peaks for the 500 nm sample reflect a higher cooperativity than for the 135 nm sample, in fair agreement with the conclusion derived from the analysis of the relaxation curves in Sec. I. The linear thermal expansion coefficients can also be determined above and below the CTCST [see Table II, Table S2 in the supplementary material and Fig. 5(b)]. In general, α_L values before and/or after thermal transitions are larger for the 135 nm sample than for the 500 nm sample (Table II). It can be noted the LTEC values reported here are consistent with volumetric thermal expansion coefficients (VTEC) reported for similar analogs.[5,35]

The above analysis implies the crystal structure of 135 nm sample is more sensitive to the environmental temperature change than the 500 nm sample, although the total volume change at CTCST is smaller than that of 500 nm sample [Fig. 5(b)]. Indeed, for the 500 nm sample, the lattice is rigid both in the high- temperature and the low-temperature regions, with limited varia- tions with respect to the temperature changes. Large linear thermal expansions are only found at the CTCST point. In contrast, the lattice shows more gradual and continuous variations of LTEC for 135 nm particles. The disordered system with smaller crystallinities in the 135 nm particles cause less cooperativity between phonons and electrons and prevent an efficient volume change at the transi- tion. The larger linear expansion coefficients with size reduction are consistent with the lowering of cooperativity when the particle size is decreased, and the gradual CTCST transitions observed for the 135 nm particles.

C. Size effects on CTCST under applied pressure

The existence of high strain inside the lattice also makes the phase transition less sensitive to the external applied pressure. Figure 6(a) shows the CTCST temperature vs applied pressure for the 135 and 500 nm samples (the *P–T* diagram for 135 nm particles was obtained by magnetic susceptibility measurement, whereas that of the 500 nm sample was extracted from diffuse reflectivity mea- surement under He gas pressure). Note that the difference of critical temperatures between the two samples is far larger than the few Kelvin shift expected using reflectivity rather than magnetometry measurements.[36] The CTCST temperature acutely shifts to higher temperatures with the external pressure for both samples. The estimated *dT/dP* values for the 135 nm sample, which were extracted

TABLE II. CTCST temperatures, linear thermal expansion coefficients, and the values of *dT/dP* for the 500 and 135 nm sample.[a]

	(1) CTCST $T_{CT1/2}$ (K)	(2) CTCST start temperature (K)	(3) LTEC at (2) (K^{-1})	(4) CTCST end temperature (K)	(5) LTEC at (4) (K^{-1})	(6) *dT/dP* on heating (K/GPa)	(7) *dT/dP* on cooling (K/GPa)
IM-A 135 nm	224.58	250	7.51×10^{-5}	185	5.66×10^{-5}	106.5	106.3
IM-B 135 nm	232.22		1.58×10^{-4}	196	5.92×10^{-5}		
IM-A 500 nm	216.71	240	9.84×10^{-5}	171	9.80×10^{-6}	215.8	236.8
IM-B 500 nm	207.04		3.87×10^{-5}	160	7.34×10^{-6}		

[a](1)–(5) were obtained from the temperature dependence of the lattice parameters in the IM state on cooling process and their linear thermal expansion coefficient analysis using formula (2). The respective (*dT/dP*) were obtained by reflectivity measurement (500 nm sample) and magnetic measurement (135 nm) under pressure.

by linear fitting, are 106.3 K/GPa along the cooling branch and 106.5 K/GPa along the heating branch (average value 106.4 K/GPa). On the other hand, for the 500 nm sample, the dT/dP values on cooling and heating are 236.8 and 215.8 K/GPa, respectively (average value 226.3 K/GPa). It should be noted that the dT/dP value of the 500 nm sample is comparable to that of the related Prussian blue analog, RbMnFe-PBA (260 K/GPa),[35] as well as for another cyanide bridged mixed-metal complex, $\{[Fe(Tp)(CN)_3]_2[Co(vbik)_2]_2\}^{2+}$, which shows a piezo-induced ETCST (electron transfer coupled to a spin transition) whose cooperativity is increased by the external pressure.37 The thermal CTCST in the 500 nm sample is more sensitive to pressure and, in fact, the thermal hysteretic behavior vanishes around 0.1 – 0.15 GPa applied pressure. These higher values of dT/dP indicate that the 500 nm sample is easily compressed because of high elasticity, which is consistent with its corresponding high α_L value during the CTCST [sharper peak in Fig. 5(b)]. While for the 135 nm particle, a higher applied pressure is required to trigger the pressure-induced CTCST because of the high internal stress in the lattice produced by the presence of small domains.
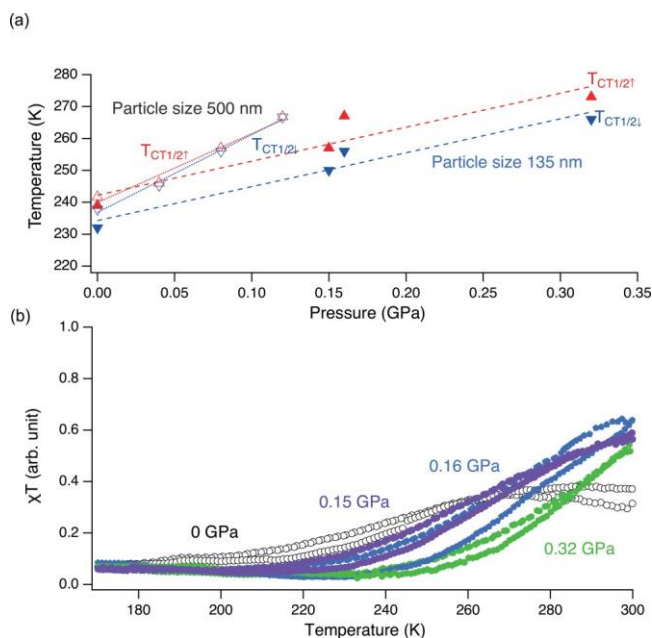

FIG. 6. (a) Pressure dependence of the CTCST temperatures for both samples. For the 135 nm sample, $T_{CT1/2\uparrow}$ (filled upward triangles) and $T_{CT1/2\downarrow}$ (filled downward triangles) are taken from the midpoints of the respective CTCST branches. For the 135 nm sample, pressure was applied at ambient temperature, and the internal pressure in the piston cylinder was monitored by the superconducting temperature of Sn. For the 500 nm sample, $T_{CT1/2\uparrow}$ (opened upward triangles) and $T_{CT1/2\downarrow}$ (opened downward triangles) are obtained by reflectivity measurement under He gas pressure. (b) CTCST behavior for the 135 nm sample under pressure measured by magnetic susceptibility. The vertical axis is expressed as arbitrary magnetic susceptibility, which is obtained after correction of the magnetic contribution of the pressure cell, calibrant, and quartz rods modeled by a linear variation (see Fig. S2 in the supplementary material).

V. CONCLUSION

An unusual IM (intermediate) phase and metastable HT (high temperature) phases in 135 nm particles of $K_{0.3}Co[Fe(CN)_6]_{0.77} \cdot nH_2O$ were investigated and compared to those of a similar sample with 500 nm particle size, by means of thermal and photo controlled PXRD and complementary magnetic susceptibility measurements. The 135 nm sample was designed to correspond to the domain size within the 500 nm sample that had earlier been shown to be comprised of mixed HT and LT (low-temperature) states, and labeled as an IM phase. The incomplete character of the thermally induced CTCST between Co^{II} ($S = 3/2$)–Fe^{III} ($S = 1/2$) and Co^{III} ($S = 0$)–Fe^{II} ($S = 0$) pairs becomes even less complete when the particle size is reduced from 500 to 135 nm. The HT Co^{II}–Fe^{III} spin states become predominant and the PXRD profiles suggest a multiphasic behavior, with a peak broadening larger than the one observed for the 500 nm sample. This behavior is attributed to HT domains or clusters made of a limited number of Co^{II}–Fe^{III} pairs that become constrained within the Co^{III}–Fe^{II} lattice at low temperatures. This lattice is thus composed of a multitude of Co^{II}–Fe^{III} clusters having different sizes and experiencing different elastic strains from the dominant Co^{III}–Fe^{II} phase. The multiple state in IM phase can be then viewed as a response of an inhomogeneous diluted system. In addition, the disordered character generated by CTCST in the 135 nm sample reflects to the LT state obtained by thermal relaxation from a single Q phase and photo-excited states from IM and LT states, these metastable states are always multiple phases.

Determination of the linear thermal expansion coefficients (LTEC) and pressure-dependent CTCST temperatures for the two (500 nm and 135 nm) particle sizes gave insights on the intrinsic stretchability and external compressibility, which indicated that the bigger sample has higher stretchability at the CTCST temperature, while the lattice change at the CTCST becomes less sensitive to external circumstances upon size reduction. We attributed these behaviors to the decrease of the cooperative electron–phonon coupling in small particles due to the enhancement of lattice defects which alters the elasticity. The weak character of the elastic energy barriers produced during photoexcitation, combined with the disorder of elastic forces in the lattice, prevents the complete photoexcitation and the collective lattice change in the 135 nm sample. As a result, in the $K_{0.3}Co[Fe(CN)_6]_{0.77} \cdot nH_2O$ compound, photoexcitation under common values of power density does not change from the multiphasic IM state and/or LT state to a single metastable HT phase, through sub-micrometer scale particle size reduction.

SUPPLEMENTARY MATERIAL

See the supplementary material for complementary experimental data: particle size distributions for $K_{0.3}Co[Fe(CN)_6]_{0.77} \cdot nH_2O$ samples (Fig. S1), $\chi.T$ vs T plot for the 135 nm KCoFe-PBA sample with a CuBe pressure cell (Fig. S2), additional PXRD data (Figs. S3 and S4) and lattice parameter change Δa (Fig. S5), time-dependent magnetic susceptibility curves of Q phase at several temperatures (Fig. S6), and M–H curves in Q and IM phases at 6 K (Fig. S7). Tables S1 and S2 indicate positions and FWHM values of (111) reflections for several phases and coefficients of a polynomial–sigmoidal function formula obtained by fitting the temperature-dependent lattice parameters of IM phases, respectively.

AUTHOR DECLARATIONS

Conflict of Interest

The authors have no conflicts to disclose.

DATA AVAILABILITY

The data that support the findings of this study are available from the corresponding author upon reasonable request.

REFERENCES

[1](a) Edward L. Wolf in *Nanophysics and Nanotechnology An Introduction to Modern Concepts in Nanoscience*, 2nd updated and enlarged ed. (Wiley-VCH Verlag GmbH & Co. KGaA, 2006), ISBN: 978-3-527-40651-7; (b) Edward L. Wolf and Manasa Medikonda in *Understanding the Nanotechnology Revolution* (Wiley-VCH Verlag GmbH & Co. KGaA, 2012), ISBN: 978-3-527-41109-2.

[2]K. A. S. Usman, J. W. Maina, S. Seyedin, M. T. Conato, L. M. Payawan, Jr., L. F. Dumée, and J. M. Razal, NPG Asia Mater. **12**, 58 (2020).

[3](a) H. Yi, R. Qin, S. Ding, Y. Wang, S. Li, Q. Zhao, and F. Pan, Adv. Funct. Mater. **31**, 2006970 (2020); (b) W. Li, C. Han, G. Cheng, S. Chou, H. Liu, and S. Dou, Small **15**, 1900470 (2019); (c) W. Ren, M. Qin, Z. Zhu, M. Yan, Q. Li, L. Zhang, D. Liu, and L. Mai, Nano Lett. **17**(8), 4713 (2017).

[4]Y. Matos-Peralta and M. Antuch, J. Electrochem. Soc. **167**, 037510 (2020).

[5](a) S. Adak, L. L. Daemen, M. Hartl, D. Williams, J. Summerhill, and H. Nakotte, J. Solid State Chem. **184**, 2854 (2011); (b) Q. Gao, N. Shi, Q. Sun, A. Sanson, R. Milazzo, A. Carnera, H. Zhu, S. H. Lapidus, Y. Ren, Q. Huang, J. Chen, and X. Xing, Inorg. Chem. **57**, 10918 (2018); (c) S. Margadonna, K. Prassides, and A. N. Fitch, J. Am. Chem. Soc. **126**, 15390 (2004); (d) A. L. Goodwin, K. W. Chapman and C. J. Kepert, J. Am. Chem. Soc. **127**, 17980 (2005); (e) T. Matsuda, J. E. Kim, K. Ohoyama, and Y. Moritomo, Phys. Rev. B **79**, 172302 (2009).

[6]K. Ikeda, S.-I. Ohkoshi, and K. Hashimoto, Chem. Phys. Lett. **349**, 371 (2001).

[7](a) O. Sato, T. Iyoda, A. Fujishima, and K. Hashimoto, Science **272**, 704 (1996); (b) O. Sato, Y. Einaga, T. Iyoda, A. Fujishima, and K. Hashimoto, J. Electrochem. Soc. **144**, L11 (1997); (c) D. A. Pejakovic, J. L. Manson, C. Kitamura, J. S. Miller, and A. J. Epstein, Polyhedron **20**, 1435 (2001); (d) C. Cartier dit Moulin, G. Champion, J. Cafun, M. Arrio, and A. Bleuzen, Angew. Chem., Int. Ed. **46**, 1287 (2007); (e) M. Hanawa, Y. Moritomo, A. Kuriki, J. Tateishi, K. Kato, M. Takata, and M. Sakata, J. Phys. Soc. Jpn. **72**, 987 (2003); (f) H. Tokoro, S. Ohkoshi, and K. Hashimoto, Appl. Phys. Lett. **82**, 1245 (2003); (g) K. Kato, Y. Moritomo, M. Takata, M. Sakata, M. Umekawa, N. Hamada, S. Ohkoshi, H. Tokoro, and K. Hashimoto, Phys. Rev. Lett. **91**, 255502 (2003).

[8]M. B. Zakaria and T. Chikyow, Coord. Chem. Rev. **352**, 328–345 (2017).

[9]X. Roy, L. K. Thompson, N. Coombs, and M. J. MacLachlan, Angew. Chem., Int. Ed. **47**, 511 (2008).

[10](a) W. Zhang, H. Song, Y. Cheng, C. Liu, C. Wang, M. Abdul, N. Khan, H. Zhang, J. Liu, C. Yu, L. Wang, and J. Li, Adv. Sci. **6**, 1801901 (2019); (b) A. Azhar, M. B. Zakaria, E. M. Ebeid, T. Chikyow, Y. Bando, A. A. Alshehri, Y. G. Alghamdi, Z. Cai, N. A. Kumar, J. Lin, H. Kim, and Y. Yamaguchi, ChemistryOpen **7**, 599 (2018); (c) M. Presle, I. Maurin, F. Maroun, R. Cortès, L. Lu, R. S. Hassan, E. Larquet, J.-M. Guigner, E. Rivière, J. P. Wright, J.-P. Boilot, and T. Gacoin, J. Phys. Chem. C **118**, 13186 (2014); (d) J. M. Cain, A. C. Felts, M. W. Meisel, and D. R. Talham, Chem. Mater. **33**, 246 (2021).

[11]D. Aguilà, Y. Prado, E. S. Koumousi, C. Mathonière, and R. Clérac, Chem. Soc. Rev. **45**, 203 (2016).

[12]M. Cammarata, S. Zerdane, L. Balducci, G. Azzolina, S. Mazerat, C. Exertier, M. Trabuco, M. Levantino, R. Alonso-Mori, J. M. Glownia, S. Song, L. Catala, T. Mallah, S. F. Matar, and E. Collet, Nat. Chem. **13**, 10 (2021).

[13]C. Chong, M. Itoi, K. Boukheddaden, E. Codjovi, A. Rotaru, F. Varret, F. A. Frye, D. R. Talham, I. Maurin, D. Chernyshov, and M. Castro, Phys. Rev. B **84**, 144102 (2011).

[14]M. J. Andrus, Y. M. Calm, E. S. Knowles, M. F. Dumont, K. A. Abboud, M. W. Meisel, and D. R. Talham, Polyhedron **64**, 289 (2013).

[15]M. Itoi, T. Jike, D. Nishino-Hamane, S. Udagawa, T. Tsuda, S. Kuwabata, K. Boukheddaden, M. J. Andrus, and D. R. Talham, J. Am. Chem. Soc. **137**, 14686 (2015).

[16]M. Itoi, I. Maurin, F. Varret, F. A. Fry, D. R. Talham, D. Chernyshov, and K. Boukheddaden, Phys. Rev. B **88**, 094104 (2013).

[17]J.-D. Cafun, L. Londinière, E. Rivière, and A. Bleuzen, Inorg. Chim. Acta **361**, 3555 (2008).

[18]Interestingly, although only two particle sizes have been studied, there could be a general scaling, as the mean dimensions of the mixed state formed by both LT and HT spin configurations is always about $\sim 1/10$ (IM-A@500 nm or IM-B@135 nm) of the total particle size, while the other domains are about $\sim 1/3$ (IM-B@500nm or IM-A@135nm).

[19](a) A. Muraoka, K. Boukheddaden, J. Linarès, and F. Varret, Phys. Rev. B **84**, 05119 (2011); (b) F. Volatron, L. Catala, E. Rivière, A. Gloter, O. Stéphan, and T. Mallah, Inorg. Chem. **47**, 6584 (2008); (c) M. Mikolasek, G. Félix, W. Nicolazzi, G. Molnár, L. Salmon, and A. Bousseksou, New. J. Chem **38**, 1834 (2014).

[20]L. Altenschmidt, G. Fornasieri, E. Rivière, F. Brisset, R. Saint-Martin, and A. Bleuzen, C. R. Chim. **22**, 508 (2019).

[21]D. M. Pajerowski, F. A. Frye, D. R. Talham, and M. W. Meisel, New J. Phys. **9**, 222 (2007).

[22]Y. Prado, L. Lisnard, D. Heurtaux, G. Rogez, A. Gloter, O. Stéphan, N. Dia, E. Rivière, L. Catala, and T. Mallah, Chem. Commun. **47**, 1051 (2011).

[23]I. Maurin, D. Chernyshov, F. Varret, A. Bleuzen, H. Tokoro, K. Hashimoto, and S.-I. Ohkoshi, Phys. Rev. B **79**, 064420 (2009).

[24]J.-H. Her, P. W. Stephens, C. M. Kareis, J. G. Moore, K. S. Min, J. Park, G. Bali, B. S. Kennon, and J. S. Miller, Inorg. Chem. **49**, 1524 (2010).

[25](a) A. Bleuzen, J.-D. Cafun, A. Bachschmidt, M. Verdaguer, P. Munsch, F. Baudelet, and J.-P. Itié, J. Phys. Chem. C **112**, 17709 (2008); (b) H. L. B. Boström, I. E. Collings, A. B. Cairns, C. P. Romao, and A. L. Goodwin, Dalton Trans. **48**, 1647 (2019); (c) H. L. B. Boström, I. E. Collings, D. Daisenberger, C. J. Ridley, N. P. Funnell, and A. B. Cairns, J. Am. Chem. Soc. **143**, 3544 (2021).

[26]Y. Moritomo, M. Hanawa, Y. Ohishi, K. Kato, M. Takata, A. Kuriki, E. Nishibori, M. Sakata, S. Ohkoshi, H. Tokoro, and K. Hashimoto, Phys. Rev. B **68**, 144106 (2003).

[27](a) T. Matsuda, J. Kim, and Y. Moritomo, Dalton Trans. **41**, 7620 (2012); (b) H. L. B. Boström and R. I. Smith, Chem. Commun. **55**, 10230 (2019).

[28](a) G. Azzolina, R. Bertoni, C. Ecolivet, H. Tokoro, S.-i. Ohkoshi, and E. Collet, Phys. Rev. B **102**, 134104 (2020); (b) E. Collet and G. Azzolina, Phys. Rev. Mater. **5**, 044401 (2020); (c) A. Slimani and K. Boukheddaden, J. Appl. Phys. **129**, 173901 (2021); (d) M. Ndiaye, N. E. I. Belmouri, J. Linares, and K. Boukheddaden, Symmetry **13**, 828 (2021).

[29](a) V. Escax, Ph.D. thesis (Université Pierre et Marie Curie, Paris, 2002); (b) V. Escax, A. Bleuzen, J.-P. Itié, P. Munsch, F. Varret, and M. Verdaguer, J. Phys. Chem. B **107**, 4763 (2003).

[30]A. C. Felts, M. J. Andrus, E. S. Knowles, P. A. Quintero, A. R. Ahir, O. N. Risset, C. H. Li, I. Maurin, G. J. Halder, K. A. Abboud, M. W. Meisel, and D. R. Talham, J. Phys. Chem. C **120**, 5420 (2016).

[31]A. Adam, M. Poggi, E. Larquet, R. Cortès, L. Martinelli, P.-E. Coulon, E. Lahera, O. Proux, D. Chernyshov, K. Boukheddaden, T. Gacoin, and I. Maurin, Nanoscale **10**, 16030 (2018).

[32]A. C. Felts, A. Slimani, J. M. Cain, M. J. Andrus, A. R. Ahir, K. A. Abboud, M. W. Meisel, K. Boukheddaden, and D. R. Talham, J. Am. Chem. Soc. **140**, 5814 (2018).

[33]W. He, J. M. Cain, M. W. Meisel, and D. R. Talham, J. Mater. Chem. C **9**, 10830 (2021).

[34]B. R. Mullaney, L. Goux-Capes, D. J. Price, G. Chastanet, J. Létard, and C. J. Kepert, Nat. Commun. **8**, 1053 (2017).

[35]K. Boukheddaden, E. D. Loutete-Dangui, E. Codjovi, M. Castro, J. A. Rodriguéz-Velamazán, S. Ohkoshi, H. Tokoro, M. Koubaa, Y. Abid, and F. Varret, J. Appl. Phys. **109**, 013520 (2011).

[36]G.-M. Rotaru, E. Codjovi, P.-R. Dahoo, I. Maurin, J. Linares, and A. Rotaru, Symmetry **13**, 1148 (2021).

[37]Y. Li, A. Benchohra, B. Xu, B. Baptiste, K. Béneut, P. Parisiades, L. Delbes, A. Soyer, K. Boukheddaden, and R. Lescouëzec, Angew. Chem. Int. Ed. **59**, 17272 (2020).